RESEARCH ARTICLE

Check for updates

Construction of multi-hydroxyl/ketone lanthanide metal–organic frameworks for understanding mechanochromic luminescence and high proton conductivity†

Baoshan Hou,‡[a] Shuyi Yang,‡[a] Bo Li,[a] Guangfu Li,[a] Haiyan Zheng,[a] Chao Qin, [ID][a] Guogang Shan, [ID][a] Zhongmin Su [ID][a,b] and Xinlong Wang [ID] *[a,b]

Two types of lanthanide metal–organic frameworks (LnMOFs) [Zr_{16}-BPDC-$Eu_{1-x}Tb_x$] and [Zr_{16}-$Eu_{1-x}Tb_x$] (x = 0.17, 0.25, 0.5) were designed and constructed through the directed assembly of multi-hydroxyl/ketone Zr-oxo clusters and Ln^{3+} ions in a single-crystal-to-single-crystal (SCSC) structural transformation manner. [Zr_{16}-BPDC-$Eu_{1-x}Tb_x$] is the first type of LnMOF to be found with mechanochromic luminescence (MCL) properties; for example, the emission color of [Zr_{16}-BPDC-$Eu_{0.83}Tb_{0.17}$] can change from yellow to orange-red when stimulated by mechanical forces, compared to which the luminescence of [Zr_{16}-$Eu_{0.83}Tb_{0.17}$] only becomes dark yellow. The proton conduction properties of [Zr_{16}-BPDC-Eu] and [Zr_{16}-Eu] were investigated because of the multi-hydroxyl/ketone character in their structures, and the proton conductivity of [Zr_{16}-Eu] was found to be 6.17×10^{-2} S cm^{-1} at 358 K and 98% relative humidity, which is the highest among hydroxyl/ketone-function MOFs. The LnMOFs with MCL and high proton conductivity pave the way to the development of more valuable properties and applications of LnMOFs.

Introduction

Self-assembly of inorganic metal ions or cluster nodes and organic linkers constitutes metal–organic frameworks (MOFs) with periodic networks and well-defined crystal structures.[1–3] Among them, luminescent metal–organic frameworks are widely used in applications such as light-emitting devices, chemosensors and bioimaging not only because the inorganic and organic parts in MOFs can provide luminescent platforms, but also the metal–ligand charge transfer and the adsorbed guest molecules in the pore channel can induce luminescence and/or add additional emission.[4–7] Lanthanide metal–organic frameworks (LnMOFs) have emerged as an excellent class of luminescent MOFs because of their unique luminescence characteristics, such as sharp line emission bands, a long luminescence lifetime, large Stokes shifts, and incredible

emission change behavior in response to a variety of external stimuli.[8,9] Carlos' group was the first to find that the fluorescence intensity of EuMOFs enhanced with increasing pH in the range of 5–7.5. Zhang *et al.* found that the emission intensity of EuMOFs decreased sharply with time under UV lamp irradiation. Then Qian and his co-workers found that mixed-lanthanide MOFs showed different fluorescence colors at different temperatures.[10–12]

Mechanochromic luminescence (MCL), in which the emissive behavior of a material is altered by external pressure stimuli or other mechanical forces, shows significant potential for applications such as fluorescence switches, information storage, and mechanosensors.[13–15] Many reported noble metal (*e.g.*, Ag^+, Pt^{2+}, and Ir^{3+}) complexes are MCL materials, and metal–metal interactions are the possible cause of MCL. Furthermore, the MCL phenomenon of MCL-active coordination polymers or MOFs originates from C–H⋯π and π–π interactions. Most of these complexes are based on Cu^+ Zn^{2+}, Cd^{2+}, and Bi^{3+}.[16–19] However, the MCL phenomenon of LnMOFs has never been discovered and studied. It is well known that when mixed-lanthanide MOFs are stimulated at different temperatures, the fluorescence colors appear different (green at low temperature and red at high temperature) due to the energy transfer from Tb^{3+} to Eu^{3+} ions.[20,21] We imagine that if mixed-lanthanide MOFs can also promote the energy transfer from Tb^{3+} to Eu^{3+} ions when stimulated by

[a]*College of Chemistry, Northeast Normal University, Changchun, China.*
E-mail: wangxl824@nenu.edu.cn
[b]*College of Science, Hainan University, Haikou, China*

†Electronic supplementary information (ESI) available: Additional characterization data, including single-crystal X-ray diffraction data, IR spectra, TGA curves, PXRD patterns, solid UV-vis spectra and photoluminescence spectra. CCDC 2171770. For ESI and crystallographic data in CIF or other electronic format see DOI: https://doi.org/10.1039/d2qi01103d
‡These authors contributed equally to this work.

4376 | *Inorg. Chem. Front.*, 2022, **9**, 4376–4384

This journal is © the Partner Organisations 2022

mechanical forces, the emission wavelength of LnMOFs will be redshifted too. When the ratio of Eu^{3+}/Tb^{3+} in mixed lanthanide MOFs is changed, a series of flexible MCL-active LnMOFs will also be obtained, and the luminescence color can change from green/yellow to orange/red when stimulated by mechanical forces, which is completely different from the abrupt two-color switching of transition metal-based MOFs whose colors before and after mechanical force stimulation cannot be expected or changed. These excellent LnMOFs with MCL characteristics need to be developed urgently.

In recent years, MOFs have received increasing attention as proton conductive materials. To obtain MOFs with higher proton conductivity, functional groups (*e.g.*, –COOH, –PO$_3$H or –SO$_3$H units) can be anchored to the host framework to enhance their acidity and hydrophilicity.[22,23] Apart from the abovementioned oxygenated acids, the exploration of hydroxyl/ketone functional groups (–OH and –C=O) as proton sources for increasing proton diffusion is still scarce.[24,25] We are interested in introducing –OH and –C=O into MOFs for proton conduction for two reasons. First, the oxygen atoms from the –OH and –C=O units in the frameworks can form complex hydrogen bond networks with the guest polar molecules (*e.g.*, H$_2$O, NH$_3$, *etc.*), which would be very favorable for proton conduction. Second, through careful modulation, the uncoordinated –OH and –C=O in MOFs will not only contribute protons, but also create an efficient proton transport pathway, which will greatly enhance proton conduction. However, so far, only a limited number of MOFs with –OH and –C=O functional groups as acidic sources or proton sources have been reported as proton conductors.

In this work, we chose Zr$_{16}$ clusters with 24 uncoordinated oxygen atoms as inorganic ligands to synthesize two types of LnMOFs by coordination with Ln^{3+} ions. A direct reaction of Zr$_{16}$ with Ln(NO$_3$)$_3$ yields [Zr$_{16}$-Eu] and [Zr$_{16}$-BPDC-Eu] is obtained by the reaction of Zr$_{16}$ with Ln(NO$_3$)$_3$ and BPDC by a new synthesis method.[26] Inspired by the different emissions of [Zr$_{16}$-BPDC-Eu$_{0.8}$Tb$_{0.2}$] at different temperatures, we investigated the luminescence characteristics of [Zr$_{16}$-BPDC-Eu$_{1-x}$Tb$_x$] (x = 0.17, 0.25, 0.5) under mechanical force stimulation. To the best of our knowledge, [Zr$_{16}$-BPDC-Eu$_{1-x}$Tb$_x$] is the first type of LnMOF reported for MCL materials, probably because of the Tb^{3+}-to-Eu^{3+} energy transfer that occurs under the stimulation of mechanical forces. Due to the presence of a large number of coordinated and uncoordinated –OH and –C=O units in [Zr$_{16}$-Eu] and [Zr$_{16}$-BPDC-Eu], we compared the proton conduction capacity of the two types of LnMOFs and found that the proton conductivity of [Zr$_{16}$-Eu] at 358 K and 98% relative humidity reached 6.17×10^{-2} S cm^{-1}, which exceeded all reported hydroxyl/ketone-function MOF crystalline materials.

Results and discussion

Structural description

Our previous work demonstrated the ability of [Zr$_{16}$] with a large number of unsaturated coordination oxygen sites that can be coordinated and assembled with metal ions (Fig. 1a). When pre-synthesized [Zr$_{16}$] crystals were soaked in a DMF solution of Eu(NO$_3$)$_3$ at 80 °C overnight, Eu^{3+} ions successfully
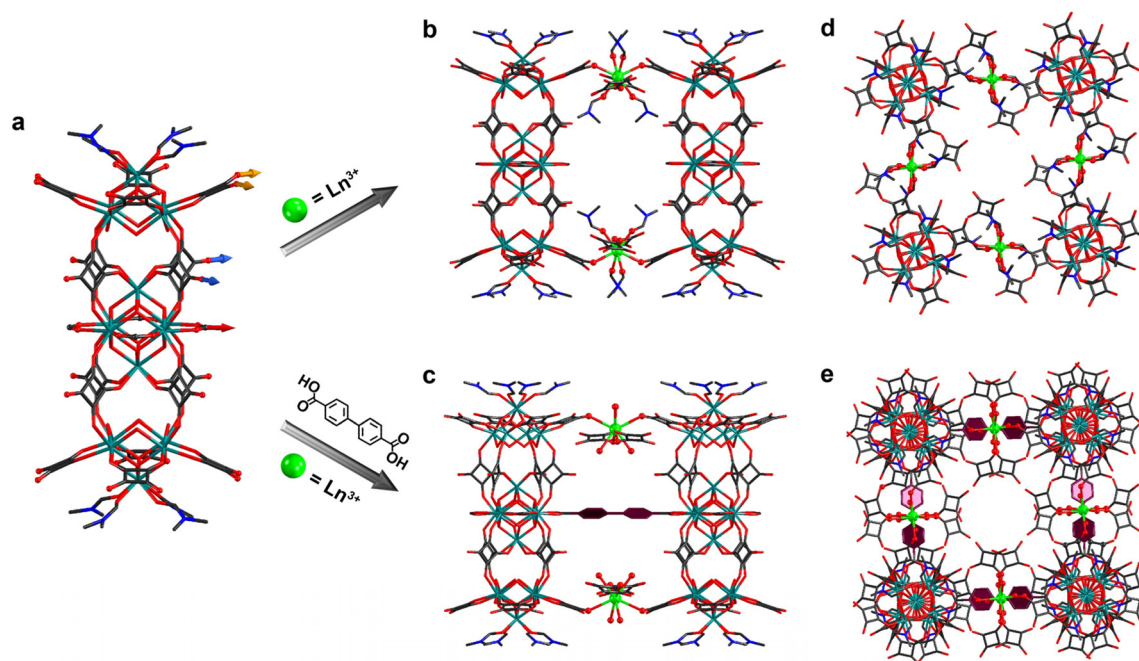

Fig. 1 (a) Crystal structure of the [Zr$_{16}$] cluster. (b and c) Magnified parts of [Zr$_{16}$-Eu] and [Zr$_{16}$-BPDC-Eu] displaying the connectivity between BPDC, Eu^{3+} ions, and [Zr$_{16}$] clusters. (d and e) Coordination details of the same layer structure in [Zr$_{16}$-Eu] and [Zr$_{16}$-BPDC-Eu].

This journal is © the Partner Organisations 2022

Inorg. Chem. Front., 2022, **9**, 4376–4384 | **4377**

coordinated to O atoms on the capped HSQA of the quadrangular pyramid $[Zr_5]$ unit in $[Zr_{16}]$ and linked the $[Zr_{16}]$ clusters into a 3D framework (Fig. 1b), $[Zr_{16}Eu(SQA)_{11}(HSQA)_5(\mu_3\text{-}OH)_{12}(\mu_3\text{-}O)_4(\mu_2\text{-}O)_8(COO)_4 (DMF)_{12}]$ (SQA = squaric acid, BPDC = 4,4′-biphenyl dicarboxylic acid, DMF = dimethylformamide) ($[Zr_{16}\text{-}Eu]$). Each Eu^{3+} ion is eight-coordinated with a dodecahedral geometry configuration, where four coordinated oxygen atoms come from the four $[Zr_{16}]$ clusters in the upper and lower layers, respectively, and the other four oxygen atoms are derived from the DMF molecule (Fig. S1a and S1b†). Interestingly, such a 0D-to-3D structural transition is carried out in a single-crystal-to-single-crystal (SCSC) manner. Compared to the crystal data of the $[Zr_{16}]$ cluster, $[Zr_{16}\text{-}Eu]$ crystallizes in the same space group $P4/mnc$ and slightly reduced cell parameters on the a/b-axis (from 19.52 to 18.58) and the c-axis (from 34.23 to 33.44) are observed, as the coordination of Eu^{3+} ions and O atoms causes the distance between $[Zr_{16}]$ clusters to become shorter.

The $[Zr_{16}]$ single crystals were placed in an $Eu(NO_3)_3$/BPDC/DMF solution overnight. X-ray single crystal diffraction clearly shows the simultaneous coordination of Ln^{3+} and BPDC with $[Zr_{16}]$ to obtain $[Zr_{16}\text{-}BPDC\text{-}Eu]$, where Eu^{3+} is coordinated to the uncoordinated oxygen atom in the HSQA of Zr_{16}, while BPDC is substituted with the mono-coordinated formic acid in Zr_{16} (Fig. 1c), demonstrating the high selectivity and precise regional distribution of the system. BPDC substituted successfully formate groups in adjacent Zr_{16} in the same layer, while Eu^{3+} ions are coordinated in approximately the same way as $[Zr_{16}\text{-}Eu]$ except that four of the coordinated oxygen atoms are from water molecules rather than DMF, probably because DMF molecules have much greater spatial resistance than water molecules, resulting in an arrangement that cannot coexist with the BPDC below (Fig. S1c and S1d†). Crystallographic analysis clearly illustrates that $[Zr_{16}\text{-}BPDC\text{-}Eu]$ crystallizes in a different space group of $I422$ compared to $[Zr_{16}]$, exhibiting slightly decreased cell parameters for the a/b axis (from 19.52 to 18.89) and the c axis (from 34.24 to 32.46). Because of the difference in the space groups of $[Zr_{16}\text{-}Eu]$ and $[Zr_{16}\text{-}BPDC\text{-}Eu]$, although they are from the same crystal system obtained by the SCSC method, the details of coordination differ significantly, where the Zr_5 cluster above and below Zr_{16} in $[Zr_{16}\text{-}BPDC\text{-}Eu]$ is distorted centered on the Zr_6 cluster, resulting in a messy arrangement compared to that of Zr_{16} in $[Zr_{16}\text{-}Eu]$ (Fig. 1d and e). The packing structures of $[Zr_{16}\text{-}Eu]$ and $[Zr_{16}\text{-}BPDC\text{-}Eu]$ are shown in Fig. S2.†

The crystallographic data table of $[Zr_{16}\text{-}Eu]$ is provided in Table S1.† The crystal purity of $[Zr_{16}\text{-}Eu]$ and $[Zr_{16}\text{-}BPDC\text{-}Eu]$ has been confirmed by highly matched powder X-ray diffraction patterns (Fig. S3 and S4†). The IR spectra and TG patterns of $[Zr_{16}\text{-}Eu]$ are shown in Fig. S5 and S6.† The Eu^{3+}/Tb^{3+} mixed lanthanide MOFs $[Zr_{16}\text{-}Eu_{1-x}Tb_x]$ and $[Zr_{16}\text{-}BPDC\text{-}Eu_{1-x}Tb_x]$ can be easily produced by changing the original molar ratio of $Eu(NO_3)_3$ and $Tb(NO_3)_3$ by the same synthesis procedure. Inductively coupled plasma spectroscopy confirmed that the molar ratio of Eu^{3+}/Tb^{3+} in the obtained $[Zr_{16}\text{-}Eu_{1-x}Tb_x]$ and $[Zr_{16}\text{-}BPDC\text{-}Eu_{1-x}Tb_x]$ matched the original molar ratio of Eu^{3+}/Tb^{3+} among synthetic raw materials.

Mechanochromic luminescence

Because of the surprising emission changes the behavior of LnMOFs in response to different stimuli and the relevance of the $[Zr_{16}\text{-}Eu]$ and $[Zr_{16}\text{-}BPDC\text{-}Eu]$ structures, the luminescence of both types of LnMOFs under mechanical force stimulation was investigated.[27,28] First we studied the luminescence behavior of $[Zr_{16}\text{-}Ln]$ and $[Zr_{16}\text{-}BPDC\text{-}Ln]$ (Ln = Eu or Tb). The emission of both compounds gradually becomes weaker with the increase of grinding time as shown in Fig. S7–S10.† The solid-state emission spectra of $[Zr_{16}\text{-}Eu_{1-x}Tb_x]$ and $[Zr_{16}\text{-}BPDC\text{-}Eu_{1-x}Tb_x]$ at room temperature were tested and as expected, all doped mixed lanthanide MOFs $[Zr_{16}\text{-}BPDC\text{-}Eu_{0.5}Tb_{0.5}]$, $[Zr_{16}\text{-}BPDC\text{-}Eu_{0.75}Tb_{0.25}]$, $[Zr_{16}\text{-}BPDC\text{-}Eu_{0.83}Tb_{0.17}]$, $[Zr16\text{-}Eu_{0.5}Tb_{0.5}]$, $[Zr16\text{-}Eu_{0.75}Tb_{0.25}]$ and $[Zr_{16}\text{-}Eu_{0.83}Tb_{0.17}]$ simultaneously show the characteristic emission of Tb^{3+} and Eu^{3+} ions. The ground samples are referred to as $[Zr_{16}\text{-}BPDC\text{-}Eu_{1-x}Tb_x]$G and $[Zr_{16}\text{-}Eu_{1-x}Tb_x]$G below. As shown in Fig. 2a, the intensity of the 544 nm characteristic peak of the Tb^{3+} ion in $[Zr_{16}\text{-}BPDC\text{-}Eu_{0.5}Tb_{0.5}]$ is much stronger than that of the 613 nm characteristic peak of the Eu^{3+} ion, emitting green luminescence, but surprisingly, the emission intensity of the Tb^{3+} ion in $[Zr_{16}\text{-}BPDC\text{-}Eu_{0.5}Tb_{0.5}]$G decreases by nearly 40%, while the emission intensity of the Eu^{3+} ion remains essentially unchanged, exhibiting yellow luminescence under 365nm irradiation (Fig. 2a). Compared with the green emission of $[Zr_{16}\text{-}BPDC\text{-}Eu_{0.75}Tb_{0.25}]$, the 544 nm emission peak of $[Zr_{16}\text{-}BPDC\text{-}Eu_{0.75}Tb_{0.25}]$G decreases sharply, while the 613 nm emission peak is enhanced and emits a slight orange light (Fig. 2b). The MCL phenomenon is most evident in $[Zr_{16}\text{-}BPDC\text{-}Eu_{0.83}Tb_{0.17}]$G, where the emission band intensity at 613 nm (Eu^{3+}) is already stronger than that at 545 nm (Tb^{3+}), emitting in orange-red, while $[Zr_{16}\text{-}BPDC\text{-}Eu_{0.83}Tb_{0.17}]$ exhibits dark yellow luminescence (Fig. 2c and S11†). However, in $[Zr_{16}\text{-}Eu_{1-x}Tb_x]$, the emission of both Eu^{3+} and Tb^{3+} ions decreases simultaneously, resulting in $[Zr_{16}\text{-}Eu_{1-x}Tb_x]$G exhibiting almost no MCL, only dimmed luminescence in the case of grinding was observed (Fig. 3a–c and S12†).

In addition, the solid absorption spectra of both types of samples before and after grinding were investigated and the corresponding data are shown in Fig. S13–S18.† The newly prepared $[Zr_{16}\text{-}Eu_{1-x}Tb_x]$ and $[Zr_{16}\text{-}BPDC\text{-}Eu_{1-x}Tb_x]$ are yellow under room light because they absorb blue light, implying a broad absorption in the range of 290–500 nm, while $[Zr_{16}\text{-}Eu_{1-x}Tb_x]$G and $[Zr_{16}\text{-}BPDC\text{-}Eu_{1-x}Tb_x]$G are white because it only absorbs UV light, indicating a stronger absorption in the range of 290–450 nm (Fig. S19 and S20†). To gain insight into the mechanochromic properties, solid-state X-ray diffraction patterns of the two types of samples before and after grinding were studied (Fig. 2d–f and 3d–f). Both $[Zr_{16}\text{-}Eu_{1-x}Tb_x]$ and $[Zr_{16}\text{-}BPDC\text{-}Eu_{1-x}Tb_x]$ pristine crystals show many strong and sharp reflection peaks, which indicate their ordered crystalline nature. Since no new diffraction peaks appear, no new crystalline phases were formed during the grinding process. However, the diffraction curves of both $[Zr_{16}\text{-}Eu_{1-x}Tb_x]$ and
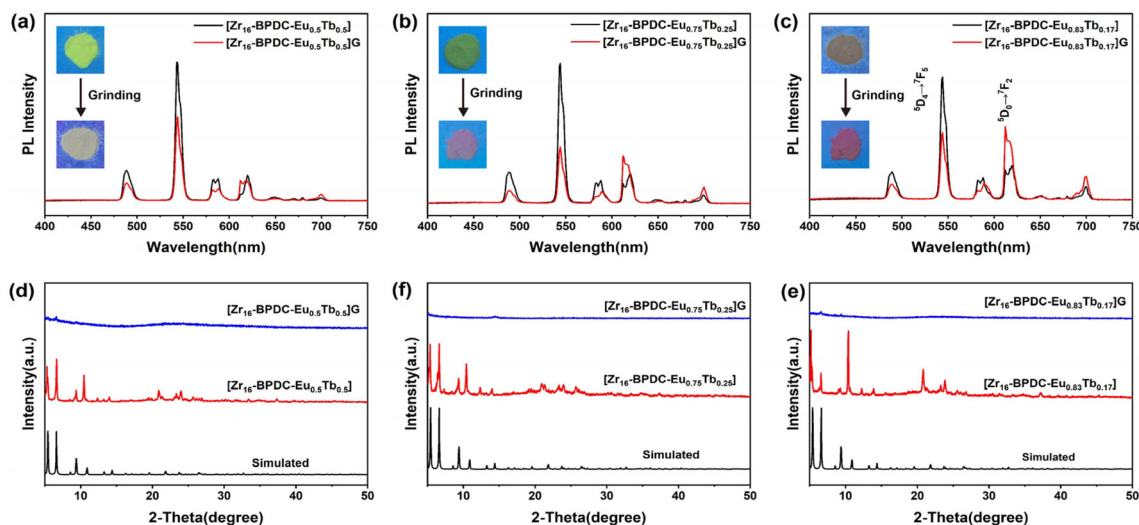
4378 | *Inorg. Chem. Front.*, 2022, **9**, 4376–4384

This journal is © the Partner Organisations 2022

Fig. 2 PL spectra of $[Zr_{16}\text{-BPDC-Eu}_{0.5}Tb_{0.5}]$ (a), $[Zr_{16}\text{-BPDC-Eu}_{0.75}Tb_{0.25}]$ (b) and $[Zr_{16}\text{-BPDC-Eu}_{0.83}Tb_{0.17}]$ (c) before and after grinding. (Inset) photographs of the three samples before and after grinding under 365 nm (UV lamp) at room temperature. Powder X-ray diffraction patterns of $[Zr_{16}\text{-BPDC-Eu}_{0.5}Tb_{0.5}]$ (d), $[Zr_{16}\text{-BPDC-Eu}_{0.75}Tb_{0.25}]$ (e) and $[Zr_{16}\text{-BPDC-Eu}_{0.83}Tb_{0.17}]$ (f) before and after grinding.
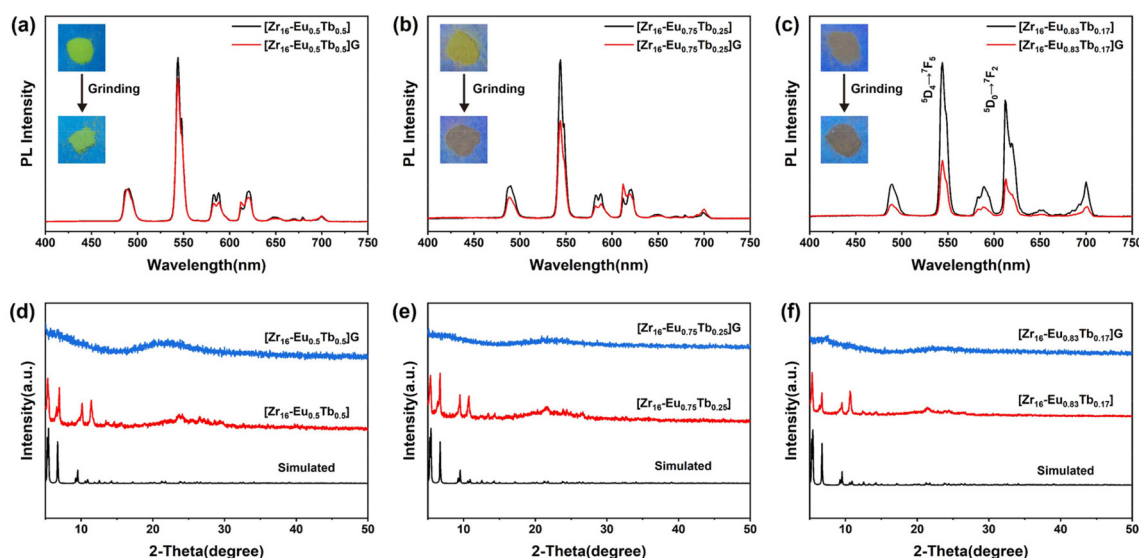
Fig. 3 PL spectra of $[\mathbf{Zr_{16}\text{-}Eu_{0.5}Tb_{0.5}}]$ (a), $[\mathbf{Zr_{16}\text{ -}Eu_{0.75}Tb_{0.25}}]$ (b) and $[\mathbf{Zr_{16}\text{-}Eu_{0.83}Tb_{0.17}}]$ (c) before and after grinding. (Inset) photographs of the three samples before and after grinding under 365 nm (UV lamp) at room temperature. Powder X-ray diffraction patterns of $[\mathbf{Zr_{16}\text{-}Eu_{0.5}Tb_{0.5}}]$ (d), $[\mathbf{Zr_{16}\text{-}Eu_{0.75}Tb_{0.25}}]$ (e) and $[\mathbf{Zr_{16}\text{-}Eu_{0.83}Tb_{0.17}}]$ (f) before and after grinding.

$[Zr_{16}\text{-BPDC-Eu}_{1-x}Tb_x]$ after grinding show weakening or disappearance of the diffraction peaks, indicating their change from the crystalline state to the amorphous state. The amorphous state produced by grinding may be caused by the disordered sliding of Zr_{16} clusters between the same layers in the structure. The FT-IR spectra before and after grinding are almost identical, indicating that the coordination bonds between the metal ions and linkers including SQA and BPDC are preserved (Fig. S21–S26†).

In order to find valuable evidence to explain the different MCL phenomena of $[Zr_{16}\text{-Eu}_{1-x}Tb_x]$ and $[Zr_{16}\text{-BPDC-Eu}_{1-x}Tb_x]$,

we tried to analyze and speculate the MCL mechanism from a structural point of view. First of all it is obvious that metal–metal interactions do not exist in these two types of structures.[29–31] Moreover, in $[Zr_{16}\text{-Eu}_{1-x}Tb_x]$ with only square acid as a ligand, there are no C–H···π and π–π interactions,[32–35] while in $[Zr_{16}\text{-BPDC-Eu}_{1-x}Tb_x]$, the BPDC between the same layer is separated by Zr_{16} clusters and the BPDC between different layers is more than 15 Å apart, which means that still there is no intermolecular interaction as mentioned above. The XRD of the amorphous state shows that the strong grinding may lead to the Zr_{16} clusters between the layers to slip, but

This journal is © the Partner Organisations 2022

Inorg. Chem. Front., 2022, **9**, 4376–4384 | **4379**

$[Zr_{16}\text{-Eu}_{1-x}Tb_x]$ does not produce the MCL phenomenon as a result, so the slip may not affect the luminescence properties in this system. Therefore, the MCL phenomenon in $[Zr_{16}\text{-}BPDC\text{-Eu}_{1-x}Tb_x]$ cannot be explained by various previous MCL mechanisms. From the solid-state emission spectra of both materials, it can be concluded that the emission centers of both are Eu^{3+} and Tb^{3+} ions, and the only difference in the structure is the BPDC linkage between the layers in $[Zr_{16}\text{-}BPDC\text{-Eu}_{1-x}Tb_x]$, which may promote the antenna effect in the structure, resulting in a more sensitive to mechanical force stimulation and promoting the energy transfer of Tb^{3+}-to-Eu^{3+} ions.

Proton conduction

Due to the presence of large quantities of uncoordinated –OH and –C=O units in the structures of both $[Zr_{16}\text{-}BPDC\text{-Eu}]$ and $[Zr_{16}\text{-Eu}]$ favoring the formation of rich hydrogen bond networks, we investigated the proton conductivity of the two samples. The crystal samples of both compounds were finely ground and pressed into small spheres for the assessment of proton conductivity at different temperatures and relative humidities by the AC impedance method. Calculations were fitted by using the ZView program to derive the values of proton conductivity. Subsequently, we analysed the proton conductivity at high relative humidities.

At 98% RH, the proton conductivity of $[Zr_{16}\text{-}BPDC\text{-Eu}]$ increased from 1.11×10^{-3} S cm^{-1} at 313 K to 1.82×10^{-2} S cm^{-1} at 358 K (Fig. 4a). The proton conductivity of $[Zr_{16}\text{-Eu}]$ increased from 2.28×10^{-4} S cm^{-1} at 303 K to 6.17×10^{-2} S cm^{-1} at 358 K (Fig. 4b). This indicates that the proton conductivity of both samples increases with temperature. This is consistent with the typical proton conducting behavior. At relatively high temperatures, they could accelerate proton motion and thus higher proton conductivity was obtained. By analyzing the structural features of two LnMOFs, it can be seen that both have a large number of –OH and –C=O units, both of which can be bound to adsorbed water molecules. Since the BPDC in $[Zr_{16}\text{-}BPDC\text{-Eu}]$ is connected between the Zr_{16} clusters in each layer, it obstructs part of the proton transport channel and also blocks the formation of a large H-bonded network. In contrast, $[Zr_{16}\text{-Eu}]$ has only Ln ions inserted between the layers of Zr_{16} and can satisfy the structural need of hydrogen bond formation by proper twisting of itself, unlike $[Zr_{16}\text{-}BPDC\text{-Eu}]$ which is fixed by Ln^{3+} ions and BPDC in both directions and is difficult to rotate. The above structural differences lead to different H-bonding networks inside the two LnMOF backbones, which further explains the different proton conduction behaviors of the two compounds. A schematic representation of the H-bonding network formed that is responsible for the proton conduction of **$[Zr_{16}\text{-Eu}]$** is shown in Fig. S27.†

Based on the Arrhenius curves obtained, the activation energies (E_a) for proton conduction in $[Zr_{16}\text{-}BPDC\text{-Eu}]$ are estimated to be 0.38 eV (313–328 K) and 0.41 eV (333–358 K) under 98% RH (Fig. 4c), indicative of the Grotthuss mecha-
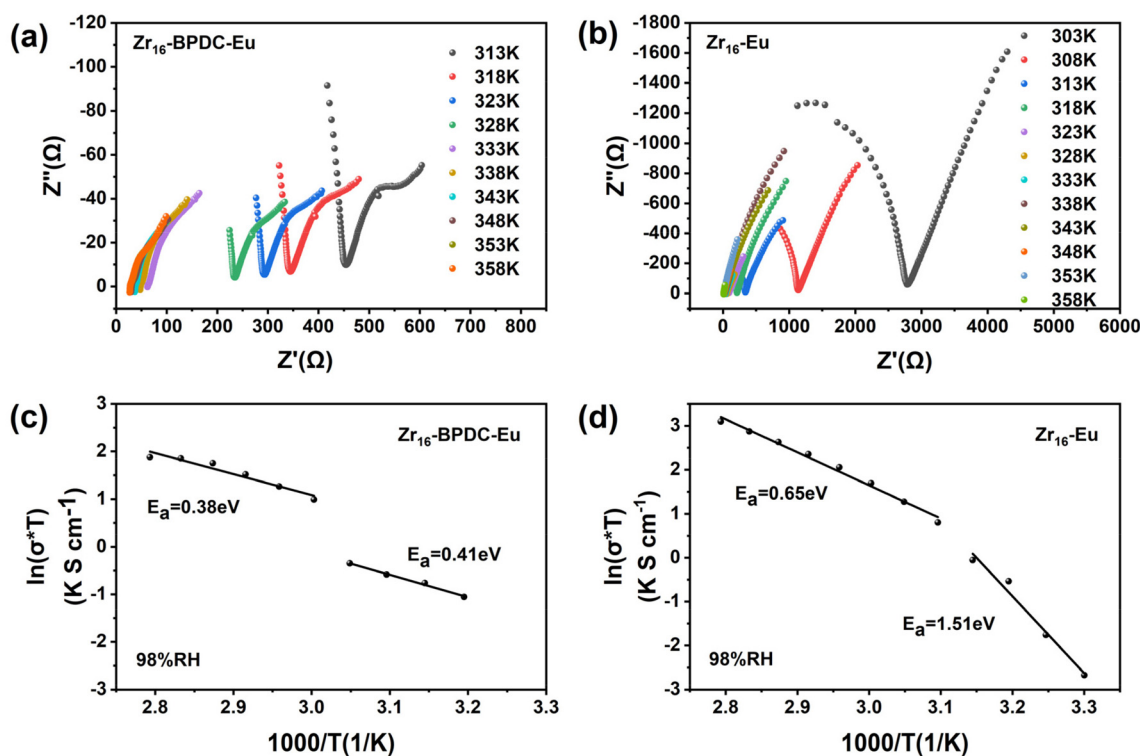

Fig. 4 Nyquist plots of **$[Zr_{16}\text{-}BPDC\text{-Eu}]$** (a) and **$[Zr_{16}\text{-Eu}]$** (b) at 98% RH and different temperatures. Arrhenius plots for the activation energy of **$[Zr_{16}\text{-}BPDC\text{-Eu}]$** (c) and **$[Zr_{16}\text{-Eu}]$** (d) at 98% RH.

4380 | *Inorg. Chem. Front.*, 2022, **9**, 4376–4384

This journal is © the Partner Organisations 2022

nism for the proton-conductive mechanism. For [Zr_{16}-Eu], the E_a value exceeds 0.40 eV and proton conduction follows the Vehicle mechanism (Fig. 4d). Moreover, note that for [Zr_{16}-BPDC-Eu] below 60% RH and [Zr_{16}-Eu] below 90% RH, the impedance pattern is irregular, collection of the relevant electrochemical data is not possible. This is probably because

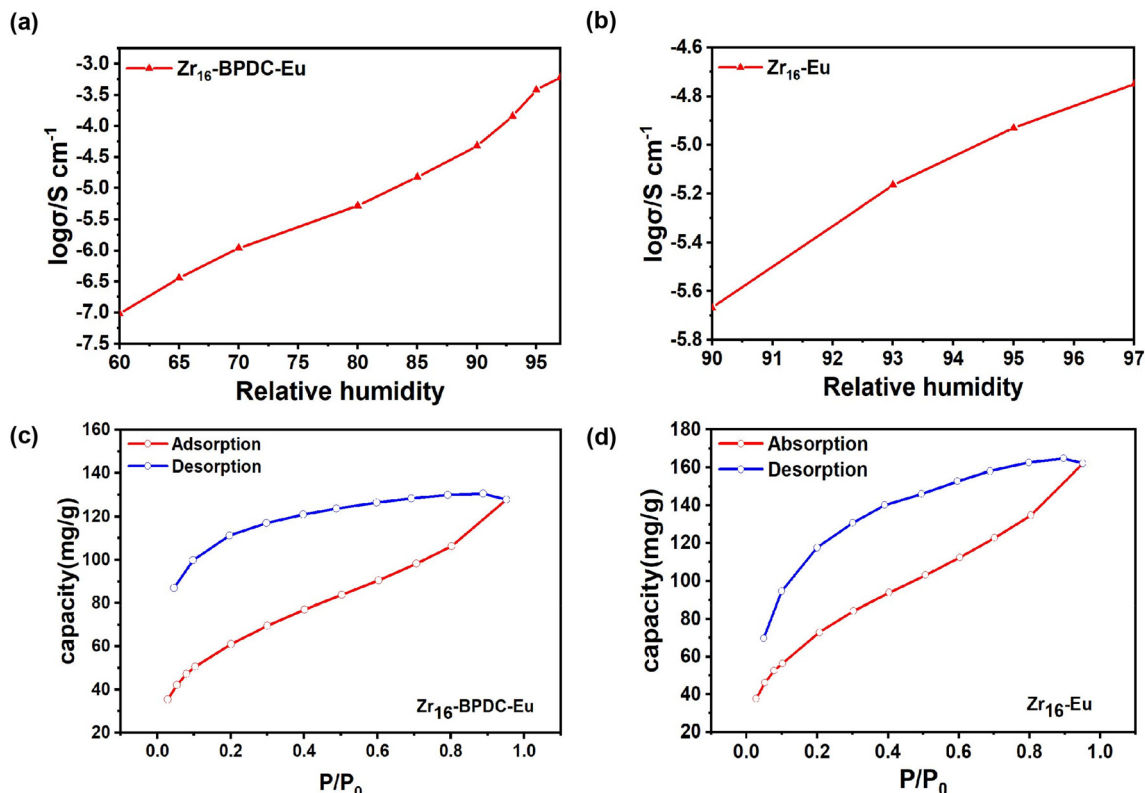**Fig. 5** Humidity dependence of proton conductivities for **[Zr_{16}-BPDC-Eu]** (a) and **[Zr_{16}-Eu]** (b). H_2O adsorption isotherms of **[Zr_{16}-BPDC-Eu]** (c) and **[Zr_{16}-Eu]** (d) at 303 K.

Table 1 Comparison of the σ values of MOFs with hydroxyl/ketone functional groups

Materials	Conductivity (S cm^{-1})	Testing conditions	Ref.
[Zr_{16}-Eu]	6.17×10^{-2}	85 °C and 98% RH	**This work**
Fe-CAT-5	5.0×10^{-2}	25 °C and 98% RH	24
PCMOF2(Pz)	4.6×10^{-2}	85 °C and 90% RH	36
FZU-1	2.84×10^{-2}	85 °C and 98% RH	37
PCMOF2-1/2	2.1×10^{-2}	85 °C and 90% RH	38
[Zr_{16}-BPDC-Eu]	1.82×10^{-2}	85 °C and 98% RH	**This work**
ZrPP-1	8.0×10^{-3}	25 °C and 98% RH	25
FZU-2	6.37×10^{-3}	85 °C and 98% RH	37
FZU-3	5.43×10^{-3}	60 °C and 98% RH	39
Hf-UiO-66(OH)$_2$	4.22×10^{-3}	100 °C and 98% RH	40
ZrPP-2	4.2×10^{-3}	25 °C and 98% RH	25
MIL-163	2.1×10^{-3}	90 °C and 95% RH	41
FZU-4	1.94×10^{-3}	60 °C and 98% RH	39
[Cu_2(Htzehp)$_2$(4,4'-bipy)]·$3H_2O$	1.43×10^{-3}	80 °C and 95% RH	42
Ti-CAT-5	8.2×10^{-4}	25 °C and 98% RH	24
HNU-3	3.61×10^{-4}	100 °C and 98% RH	43
HNU-1	2.24×10^{-4}	100 °C and 98% RH	43
HNU-2	2.00×10^{-4}	100 °C and 98% RH	43
[Ca(tart)]$_n$·$4n(H_2O)$	3.0×10^{-5}	25 °C and 100% RH	44
Zn_4(5-mtz)$_4$(L-mal)$_2$(H_2O)$_2$	1.33×10^{-5}	60 °C and 95% RH	45
(Cs$_3$(THB)(H_2O)$_{3.4}$ (S-12)	1.1×10^{-5}	70 °C and 50% RH	46
Al(OH)(bdc-OH)(H_2O)$_{1.5}$[MIL-53(Al)-OH]	1.9×10^{-6}	80 °C and 95% RH	47
[Cd(L-tart)(4,4'-bipy)(H_2O)]$_n$·$9n(H_2O)$	1.3×10^{-6}	85 °C and 95% RH	48
[Cd(D-tart)(4,4'-bipy)(H_2O)]$_n$·$9n(H_2O)$	1.3×10^{-6}	85 °C and 95% RH	48
[Cd(DL-tart)(4,4'-bipy)(H_2O)]$_n$·$6n(H_2O)$	4.5×10^{-7}	85 °C and 95% RH	48

This journal is © the Partner Organisations 2022

Inorg. Chem. Front., 2022, **9**, 4376–4384 | **4381**

under low RH conditions the skeleton absorbs fewer water molecules which is not enough to form a sufficient network of H-bonds to act as a good proton transfer. Therefore, proton conductivity measurements were performed for [Zr_{16}-BPDC-Eu] under 60%, 65%, 70%, 80%, 85%, 90%, 93%, 95% and 97% RHs (Fig. 5a) at 303 K and for [Zr_{16}-Eu] under 90%, 93%, 95% and 97% RHs (Fig. 5b). The proton conductivity of [Zr_{16}-BPDC-Eu] increased from 9.52×10^{-8} S cm^{-1} at 60% RH to 6.09×10^{-4} S cm^{-1} at 97% RH, and that of [Zr_{16}-Eu] increased from 2.15×10^{-6} S cm^{-1} at 90% RH to 1.78×10^{-5} S cm^{-1} at 97% RH. The proton conductivity of the two samples increased as the RH increased, which shows that the proton-conductive behavior is typically mediated by water. As the relative humidity increases, the number of water molecules attached to the skeleton also increases, leading to an increase in the number of proton carriers. Based on the above data, we conclude that the optimum proton conductivity for both [Zr_{16}-BPDC-Eu] and [Zr_{16}-Eu] is more than 10^{-2} S cm^{-1}, indicating that both samples have a high proton conductivity. When the RH increases, the H_2O units enter the skeleton and interact with the uncoordinated –OH and –C=O groups in the square acid to establish hydrogen bond networks. On the other hand, they act as proton carriers for proton transfer, which leads to an efficient enhancement of proton transport. To demonstrate this, H_2O adsorption/desorption experiments have been carried out for [Zr_{16}-BPDC-Eu] and [Zr_{16}-Eu] and curves of the water adsorption/desorption isotherms have been plotted (Fig. 5c and d). The water vapor adsorption isotherms of [Zr_{16}-BPDC-Eu] and [Zr_{16}-Eu] at 303 K showed the maximum uptake of 127.81 and 162.14 mg g^{-1}, respectively. At higher relative humidity, both samples could accommodate more water molecules in the framework due to the hydrophilic nature of the –OH and –C=O units, which was confirmed by the fact that the samples exhibited higher conductivity at higher relative humidity. As shown in Table 1, the σ value of [Zr_{16}-Eu] is impressive and exceeds that of almost all multi-hydroxyl/ketone MOFs under similar conditions. This indicates that the strategy of choosing multi-hydroxyl/ketone ligands to synthesize MOFs with high proton conductivity is successful. Finally, we tested the stability of proton conductivity for [Zr_{16}-BPDC-Eu] and [Zr_{16}-Eu] and the conductivity of both samples is basically unchanged after 300 min (Fig. S28 and S29†).

Conclusion

In summary, we have selected Zr clusters with –OH and –C=O groups as inorganic ligands to synthesize two types of LnMOFs, realizing the 0D-to-3D structural transition by SCSC structural transformation. Among them [Zr_{16}-BPDC-Eu$_{1-x}$Tb$_x$] is the first reported case of LnMOFs with MCL properties, stemming from a new MCL mechanism also known as Tb^{3+}-to-Eu^{3+} energy transfer. The development of this MCL material has changed the situation of single two-color switching, and by changing the ratio of starting Ln^{3+} ions, we can manipulate different color transitions under the stimulation of mechanical

forces. Moreover, the ultra-high proton conductivity of [Zr_{16}-Eu] surprised us, reaching 6.17×10^{-2} S cm^{-1}, exceeding all hydroxyl/ketone-mediated MOFs, confirming the great potential of proton-conducting materials with hydroxyl/ketone functional groups as proton sources. This work represents a significant advancement in the field of MCL materials and provides a new synthetic strategy for the preparation of novel crystalline MOFs with the desired functionality.

Conflicts of interest

The authors declare no competing financial interest.

Acknowledgements

References

1 Q. Liu, Y. Y. Song, Y. H. Ma, Y. Zhou, H. J. Cong, C. Wang, J. Wu, G. L. Hu, M. O'Keeffe and H. X. Deng, Mesoporous Cages in Chemically Robust MOFs Created by a Large Number of Vertices with Reduced Connectivity, *J. Am. Chem. Soc.*, 2019, **141**, 488–496.

2 Z. J. Chen, Z. Thiam, A. Shkurenko, L. J. Weselinski, K. Adil, H. Jiang, D. Alezi, A. H. Assen, M. O'Keeffe and M. Eddaoudi, Enriching the Reticular Chemistry Repertoire with Minimal EdgeTransitive Related Nets: Access to Highly Coordinated Metal–Organic Frameworks Based on Double Six-Membered Rings as NetCoded Building Units, *J. Am. Chem. Soc.*, 2019, **141**, 20480–20489.

3 V. Guillerm, T. Grancha, I. Imaz, J. Juanhuix and D. Maspoch, Zigzag Ligands for Transversal Design in Reticular Chemistry: Unveiling New Structural Opportunities for Metal–Organic Frameworks, *J. Am. Chem. Soc.*, 2018, **140**, 10153–10157.

4 B. Wang, P. L. Wang, L. H. Xie, R. B. Lin, J. Lv, J. R. Li and B. L. Chen, A stable zirconium based metal-organic framework for specific recognition of representative polychlorinated dibenzo-p-dioxin molecules, *Nat. Commun.*, 2019, **10**, 3861.

5 C. Y. Sun, X. L. Wang, X. Zhang, C. Qin, P. Li, Z. M. Su, D. X. Zhu, G. G. Shan, K. Z. Shao, H. Wu and J. Li, Efficient and tunable white-light emission of metal–organic frameworks by iridium-complex encapsulation, *Nat. Commun.*, 2013, **4**, 2717.

6 Y. J. Cui, J. Zhang, H. J. He and G. D. Qian, Photonic functional metal–organic frameworks, *Chem. Soc. Rev.*, 2018, **47**, 5740–5785.

7 A. Mallick, A. M. El-Zohry, O. Shekhah, J. Yin, J. T. Jia, H. Aggarwal, A. H. Emwas, O. F. Mohammed and M. Eddaoudi, Unprecedented Ultralow Detection Limit of Amines using a Thiadiazole-Functionalized Zr(IV)-Based

4382 | *Inorg. Chem. Front.*, 2022, **9**, 4376–4384

This journal is © the Partner Organisations 2022

Metal–Organic Framework, *J. Am. Chem. Soc.*, 2019, **141**, 7245–7249.

8 Y. Y. Ou, W. J. Zhou, Z. C. Zhu, F. K. Ma, R. F. Zhou, F. Su, L. R. Zheng, L. Ma and H. B. Liang, Host Differential Sensitization toward Color/Lifetime-Tuned Lanthanide Coordination Polymers for Optical Multiplexing, *Angew. Chem., Int. Ed.*, 2020, **59**, 23810–23816.

9 Z. Q. Li, G. N. Wang, Y. X. Ye, B. Li, H. R. Li and B. L. Chen, Loading Photochromic Molecules into a Luminescent Metal–Organic Framework for Information Anticounterfeiting, *Angew. Chem., Int. Ed.*, 2019, **58**, 18025–18031.

10 C. D. S. Brites, P. P. Lima, N. J. O. Silva, A. Millán, V. S. Amaral, F. Palacio and L. D. Carlos, A Luminescent Molecular Thermometer for Long-Term Absolute Temperature Measurements at the Nanoscale, *Adv. Mater.*, 2010, **22**, 4499–4504.

11 J. K. Sun, L. X. Cai, Y. J. Chen, Z. H. Li and J. Zhang, Reversible luminescence switch in a photochromic metal–organic framework, *Chem. Commun.*, 2011, **47**, 6870–6872.

12 Y. J. Cui, H. Xu, Y. F. Yue, Z. Y. Guo, J. C. Yu, Z. X. Chen, J. K. Gao, Y. Yang, G. D. Qian and B. L. Chen, A Luminescent Mixed-Lanthanide Metal–Organic Framework Thermometer, *J. Am. Chem. Soc.*, 2012, **134**, 3979–3982.

13 Q. Zhang, J. Su, D. W. Feng, Z. W. Wei, X. D. Zou and H. C. Zhou, Piezofluorochromic Metal–Organic Framework: A Microscissor Lift, *J. Am. Chem. Soc.*, 2015, **137**, 10064–10067.

14 X. Han, J. L. Tong, G. Y. Ding, C. Y. Sun, X. L. Wang, Z. M. Su, J. Sun, L. L. Wen and G. G. Shan, Highly emissive coordination polymer derived from tetraphenylethylene-tetrazole chromophore: synthesis, characterization and piezochromic luminescent behavior, *Chin. Chem. Lett.*, 2022, DOI: 10.1016/j.cclet.2022.02.060, Just Published.

15 B. C. Tzeng, T. Y. Chang and H. S. Sheu, Reversible Phase Transformation and Luminescent Mechanochromism of ZnII-Based Coordination Frameworks Containing a Dipyridylamide Ligand, *Chem. – Eur. J.*, 2010, **16**, 9990–9993.

16 H. Wu, S. Q. Zhang and L. Zhao, Multiresponsive Luminescent Behaviors of Assembled Spirocyclic Nonanuclear Silver(I) Clusters, *CCS Chem.*, 2022, DOI: 10.31635/ccschem.021.202101229, Just Published.

17 G. F. Li, T. Z. Yang, K. Z. Shao, Y. Gao, G. G. Shan, Z. M. Su, X. L. Wang and D. X. Zhu, Understanding Mechanochromic Luminescence on Account of Molecular Level Based on Phosphorescent Iridium(III) Complex Isomers, *Inorg. Chem.*, 2021, **60**, 3741–3748.

18 D. X. Zhang, H. X. Zhang, T. Wen, D. S. Li and J. Zhang, Mechanochromic Cu(I) boron imidazolate frameworks with low-dimensional structures and reducing function, *Inorg. Chem. Front.*, 2016, **3**, 263–267.

19 O. Toma, M. Allain, F. Meinardi, A. Forni, C. Botta and N. Mercier, Bismuth-Based Coordination Polymers with Efficient Aggregation-Induced Phosphorescence and Reversible Mechanochromic Luminescence, *Angew. Chem., Int. Ed.*, 2016, **55**, 7998–8002.

20 X. T. Rao, T. Song, J. K. Gao, Y. J. Cui, Y. Yang, C. D. Wu, B. L. Chen and G. D. Qian, A Highly Sensitive Mixed Lanthanide Metal–Organic Framework Self-Calibrated Luminescent Thermometer, *J. Am. Chem. Soc.*, 2013, **135**, 15559–15564.

21 Y. J. Cui, W. F. Zou, R. J. Song, J. C. Yu, W. Q. Zhang, Y. Yang and G. D. Qian, A ratiometric and colorimetric luminescent thermometer over a wide temperature range based on a lanthanide coordination polymer, *Chem. Commun.*, 2014, **50**, 719–721.

22 X. X. Xie, Y. C. Yang, B. H. Dou, Z. F. Li and G. Li, Proton conductive carboxylate-based metal–organic frameworks, *Coord. Chem. Rev.*, 2019, **403**, 213100.

23 S. S. Bao, G. K. H. Shimizu and L. M. Zheng, Proton conductive metal phosphonate frameworks, *Coord. Chem. Rev.*, 2017, **378**, 577–594.

24 E. X. Chen, G. Xu and Q. P. Lin, Robust Porphyrin-Spaced Zirconium Pyrogallate Frameworks with High Proton Conduction, *Inorg. Chem.*, 2019, **58**, 3569–3573.

25 N. T. T. Nguyen, H. Furukawa, F. Gándara, C. A. Trickett, H. M. Jeong, K. E. Cordova and O. M. Yaghi, Three-Dimensional Metal-Catecholate Frameworks and Their Ultrahigh Proton Conductivity, *J. Am. Chem. Soc.*, 2015, **137**, 15394–15397.

26 B. S. Hou, C. Qin, C. Y. Sun, X. L. Wang and Z. M. Su, Stepwise Construction of Multivariate Metal–Organic Frameworks from a Predesigned Zr16 Cluster, *CCS Chem.*, 2021, **3**, 287–293.

27 J. Y. Ren, Z. Niu, Y. X. Ye, C. Y. Tsai, S. X. Liu, Q. Z. Liu, X. Q. Huang, A. Nafady and S. Q. Ma, Second-Sphere Interaction Promoted Turn-On Fluorescence for Selective Sensing of Organic Amines in a TbIII-based Macrocyclic Framework, *Angew. Chem., Int. Ed.*, 2021, **60**, 23705–23712.

28 G. P. Li, H. F. Xie, P. F. Hao, Y. L. Fu, K. Zhang, J. J. Shen and Y. Y. Wang, Size Effect of Arylenediimide π–Conjugate Systems on the Photoresponsive Behaviors in Eu³⁺-Based Coordination Polymers, *Inorg. Chem.*, 2022, **61**(17), 6403–6410.

29 S. Perruchas, X. F. L. Goff, S. Maron, I. Maurin, F. Guillen, A. Garcia, T. Gacoin and J. P. Boilot, Mechanochromic and Thermochromic Luminescence of a Copper Iodide Cluster, *J. Am. Chem. Soc.*, 2010, **132**, 10967–10969.

30 X. Q. Zhang, Z. G. Chi, Y. Zhang, S. W. Liu and J. R. Xu, Recent Advances in Mechanochromic Luminescent Metal Complexes, *J. Mater. Chem. C*, 2013, **1**, 3376–3390.

31 T. Wen, X. P. Zhou, D. X. Zhang and D. Li, Luminescent Mechanochromic Porous Coordination Polymers, *Chem. – Eur. J.*, 2014, **20**, 644–648.

32 L. X. Hu, M. Y. Gao, T. Wen, Y. Kang and S. M. Chen, Synthesis of Halide-Modulated Cuprous(I) Coordination Polymers with Mechanochromic and Photocatalytic Properties, *Inorg. Chem.*, 2017, **56**, 6507–6511.

33 Y. Yan, N. N. Zhang, R. Li, J. G. Xu, J. Lu, F. K. Zheng and G. C. Guo, Coordination Polymers with Grinding-Size-Dependent Mechanoresponsive Luminescence Induced by

This journal is © the Partner Organisations 2022

Inorg. Chem. Front., 2022, **9**, 4376-4384 | **4383**

π⋯π Stacking Interactions, *Eur. J. Inorg. Chem.*, 2017, 3811–3814.

34 Y. Yan, J. Chen, N. N. Zhang, M. S. Wang, C. Sun, X. S. Xing, R. Li, J. G. Xu, F. K. Zheng and G. C. Guo, Grinding Size-dependent Mechanoresponsive Luminescent Cd(II) Coordination Polymer, *Dalton Trans.*, 2016, **45**, 18074–18078.

35 J. J. Liu, S. B. Xia, Q. T. Que, H. B. Suo, J. M. Liu, X. Shen and F. X. Cheng, Naphthalimide-containing Coordination Polymer with Mechanoresponsive Luminescence and Excellent Metal Ion Sensing Properties, *Dalton Trans.*, 2020, **49**, 3174–3180.

36 S. Kim, B. Joarder, J. A. Hurd, J. Zhang, K. W. Dawson, B. S. Gelfand, N. E. Wong and G. K. H. Shimizu, Achieving Superprotonic Conduction in Metal–Organic Frameworks through Iterative Design Advances, *J. Am. Chem. Soc.*, 2018, **140**(3), 1077–1082.

37 L. D. Lin, Z. Li, D. Zhao, J. H. Liu, X. X. Li and S. T. Zheng, Development of a new Lindqvist-like Fe6 cluster secondary building unit for MOFs, *Chem. Commun.*, 2019, **55**, 10729–10732.

38 S. Kim, K. W. Dawson, B. S. Gelfand, J. M. Taylor and G. K. Shimizu, Enhancing Proton Conduction in a Metal–Organic Framework by Isomorphous Ligand Replacement, *J. Am. Chem. Soc.*, 2013, **135**, 963–966.

39 L. D. Lin, Z. Li, J. H. Liu, Y. Q. Sun, X. X. Li and S. T. Zheng, A new type of composite MOFs based on high-valent Sb(v)-based units and cuprous-halide clusters, *Chem. Commun.*, 2019, **55**, 15113–15116.

40 X. Chen, S. Z. Wang, S. H. Xiao, Z. F. Li and G. Li, High Protonic Conductivity of Three Highly Stable Nanoscale Hafnium(IV) Metal–Organic Frameworks and Their Imidazole-Loaded Products, *Inorg. Chem.*, 2022, **61**, 4938–4947.

41 P. G. M. Mileo, S. D. Vinot, G. Mouchaham, F. Faucher, N. Guillou, A. Vimont, C. Serre and G. Maurin, Proton-Conducting Phenolate-Based Zr Metal–Organic Framework: A Joint Experimental–Modeling Investigation, *J. Phys. Chem. C*, 2016, **120**, 24503–24510.

42 R. Li, S. H. Wang, X. X. Chen, J. Lu, Z. H. Fu, Y. Li, G. Xu, F. K. Zheng and G. C. Guo, Highly Anisotropic and Water Molecule-Dependent Proton Conductivity in a 2D Homochiral Copper(II) Metal–Organic Framework, *Chem. Mater.*, 2017, **29**, 2321–2331.

43 H. Yang, X. Y. Duan, J. J. Lai, Y. Zhao, X. J. Wang and M. L. Wei, Proton-Conductive Cocrystals of Twin Isomers of Coordination Polymers in Situ Formed by Keggin Anions and Cu(II)-4,4′-Bis(hydroxymethyl)-2,2′-bipyridine Complex Moieties, *Inorg. Chem.*, 2019, **58**, 446–455.

44 D. Saravanabharathi, M. Obulichetty, S. Rameshkumar and M. Kumaravel, Humidity based proton conductivity of calcium-l-tartrate tetrahydrate: An environmentally benign coordination polymer as a solid electrolyte, *Synth. Met.*, 2014, **196**, 76–82.

45 M. Y. Li, F. Wang and J. Zhang, Synthesis, structure and proton conductivity of a metal–organic framework with rich hydrogen-bonds between the layers, *Inorg. Chem. Commun.*, 2017, **79**, 37–40.

46 N. Wong, J. A. Hurd, R. Vaidhyanathan and G. K. H. Shimizu, A proton-conducting cesium sulfonate metal organic framework, *Can. J. Chem.*, 2015, **93**, 988–991.

47 A. Shigematsu, T. Yamada and H. Kitagawa, Wide Control of Proton Conductivity in Porous Coordination Polymers, *J. Am. Chem. Soc.*, 2011, **133**, 2034–2036.

48 S. Parshamoni, H. S. Jena, S. Sanda and S. Konar, Synthesis, characterisation, water adsorption and proton conductivity of three Cd(ii) based luminescent metal–organic frameworks, *Inorg. Chem. Front.*, 2014, **1**, 611–620.

4384 | *Inorg. Chem. Front.*, 2022, **9**, 4376–4384

This journal is © the Partner Organisations 2022